Power Electronic Systems
Laboratory

IEEE/ASME Transactions on Mechatronics, Vol. 20, No. 3, pp. 1149-1159, June 2015

Multivariable State Feedback Control of a 500 000-r/min Self-Bearing Permanent-Magnet Motor

T. Baumgartner,
J.W.Kolar

Eidgenössische Technische Hochschule Zürich
Swiss Federal Institute of Technology Zurich

Multivariable State Feedback Control of a 500 000-r/min Self-Bearing Permanent-Magnet Motor

Thomas Baumgartner, *Student Member, IEEE*, and Johann W. Kolar, *Fellow, IEEE*

***Abstract*—The use of magnetic bearings in electrical drive systems enables very long lifetimes at highest speeds and the operation in high-purity or vacuum environments. The machine prototype presented in this paper overcomes several limitations of previously presented high-speed magnetically levitated electrical drive systems. The design features linear bearing characteristics, which enables applying linear state feedback control without linearization of bearing actuators. A multivariable rotor position control scheme is proposed and implemented on a signal processor. The implemented Kalman filter and the linear state feedback controller proved to perform well in practice, stabilizing the system over the design speed range of the machine with a single set of controller parameters. Closed-loop system transfer function measurements verify the presented system modeling and controller performance. Measurements of the machine spinning at 500 000 r/min verify the functionality of the overall system. To the authors' knowledge, this is the highest speed achieved by magnetically levitated electrical drive systems so far.**

***Index Terms*—Active magnetic bearing (AMB), high-speed magnetic bearing, Kalman filter, linear quadratic Gaussian (LQG), linear quadratic regulator (LQR), state feedback control, vacuum.**

I. Introduction

In the last few years, several studies dealing with the design of high-speed electrical drive systems have been published, e.g., [1], [2]. The scaling and the speed limitations of high-speed electrical machines are analyzed in [3]–[5]. However, the use of ultrahigh-speed systems in industrial applications has been limited, mainly by the absence of reliable bearings for rotor support and long lifetime of several thousand hours. Promising candidates for high-speed bearings with longer lifetimes are contactless concepts such as active magnetic bearings (AMB) or gas bearings. The scope of this paper is the magnetic bearing, as it is the only contactless bearing technology that can be operated in vacuum or low-pressure environments, such as high-speed optical scanning systems or reaction wheels for attitude control of satellites in orbit. The focus will be on low-power ultrahigh-speed electrical drive systems.

Most AMB systems built today rely on reluctance force which is generated by guiding a magnetic flux over the air gap between the rotor and the stator. This flux is actively controlled by controlling the bearing winding currents. In this paper, this bearing topology will be referred to as reluctance-force-based AMB. In contrast, Lorentz-force-based AMB rely on an external magnetic flux density (typically generated by a set of permanent magnets on the rotor) and electric current densities in bearing windings. The windings are placed in the magnetic air gap of the external flux density. Thus, the bearing force generation is mainly based on Lorentz force in the bearing windings [6], [7].

A magnetically levitated 60 krpm flywheel system is presented in [8]. Given the large diameter of the flywheel rim, the maximum tip speed is 700 m/s. Several magnetic bearing concepts for rotational speeds beyond 100 000 revolutions per minute (rpm) have been investigated recently. Reluctance-force-based homopolar bearings are presented in [9] and [10]. In [9], a magnetically levitated milling spindle is presented that achieved a speed of 150 krpm. In [10], a 2-kW machine was operated up to a speed of 120 krpm. In [11], a combined radial-axial reluctance-force-based bearing is presented that was tested up to 120 krpm. A spinning unit that was used for yarn production with speeds of up to 140 krpm is reported in [12]. However, one of the limitations of achievable actuator bandwidth of reluctance-force-based AMB follows from eddy currents in the lamination of the magnetic circuit [13]. Furthermore, slot harmonic-induced iron losses in the rotor increase with the rotational speed [13], [14]. Due to the poor thermal coupling of the levitated rotor to the rest of the drive system, these losses are crucial. Therefore, a downscaling of a reluctance-force-based AMB system to reach higher rotational speeds is limited among others factors by the high rotor losses.

The maximum bearing force of slotless and thus Lorentz-force-based AMB systems is small compared to reluctance-force-based AMB systems [6]. While the lower bearing force is typically not a concern in optical applications, it becomes a limiting factor in applications with high bearing loads such as milling applications. On the other hand, the slotless design of the windings allows controlling bearing forces up to high bandwidths [7]. Furthermore, low rotor losses enable high-speed rotation. Self-bearing[1] motors feature an integrated design of the motor and the magnetic bearing which reduces the total length of the rotor when compared to nonintegrated AMB systems.

Manuscript received July 15, 2013; revised November 20, 2013; accepted April 28, 2014. Date of publication April 27, 2014; date of current version May 18, 2015. Recommended by Technical Editor M. de Queiroz.

The authors are with the Power Electronic Systems Laboratory, Swiss Federal Institute of Technology (ETH) Zurich, CH-8092 Zurich, Switzerland (e-mail: baumgartner@lem.ee.ethz.ch; kolar@lem.ee.ethz.ch).

Color versions of one or more of the figures in this paper are available online at http://ieeexplore.ieee.org.

Digital Object Identifier 10.1109/TMECH.2014.2323944

[1]The alternative term *bearingless* can be found in the literature. However, even though self-bearing/bearingless machines use a common magnetic circuit for bearing force and drive torque generation, some designs feature dedicated bearing windings. Therefore, the term *bearingless* might be misleading. Thus, the term *self-bearing* is used throughout this paper.

The length reduction increases the bending mode frequencies which is beneficial for rotor dynamics of high-speed motors [13]. The drawbacks of self-bearing concepts are the generally higher system complexity. Furthermore, typically, the bearing currents have to be controlled in field-oriented coordinates.

Similarly to the machine concept proposed in this paper, a slotless and thus Lorentz-force-based high-speed self-bearing motor is presented in [15]. In contrast to the proposed design, a short (slice) rotor was chosen. Therefore, only two degrees of freedom (DOF) have to be controlled by the magnetic bearing. One DOF is controlled by the motor, and three DOFs are stabilized passively by the reluctance force. The maximum achieved speed of 115 krpm is limited by the mechanical construction of the rotor [15]. A downscaling of the dimensions of the slice motor to reach higher rotational speeds is limited by the passive stabilization of three DOFs. The slotless self-bearing motor was proposed in [16] and [17] and applied to lower speed applications [18]–[21].

A large variety of methods are proposed in the literature for the control of AMB [13]. Generally, a fair and credible comparison of control methods is a very difficult task, as the control performance highly depends on the selection of control parameters. Furthermore, different mechanical machine topologies complicate the comparison additionally. A comparison between centralized and decentralized and also between proportional integral derivative (PID) and linear quadratic (LQ) control methods is presented in [22]. In all cases that were studied in [22], the centralized model-based controllers performed better when compared with the decentralized PID-based solutions.

In many AMB systems built today, particularly in industrial practice, PID regulators are implemented, e.g., [11], [23]–[25]. Typically, different regulators are used for different states of the multiple-input multiple-output (MIMO) control problem. Most control algorithms require information of system states like radial rotor velocities. Typically, these states cannot be measured directly with the employed rotor position sensor. Therefore, nonobserver-based control structures are prone to high-frequency measurement noise that is amplified by the differential part of the controller [26].

The authors of [26] showed that the control performance and the measurement noise rejection of an AMB system can be significantly improved by applying linear quadratic Gaussian (LQG) control algorithm for decentralized magnetic bearing control. In [27], LQ control is presented that is based on a flexible rotor model for an AMB system employing nonlinear bearing actuators. A linear-quadratic-regulator (LQR)-based control of a Lorentz-force-type actuator is proposed in [28]. In [29], several approaches (including LQR) for the control of a flywheel energy storage device are analyzed. A cross feedback control was selected in [29] due to the strong gyroscopic couplings.

In 1946, a rotational speed of 23 million rpm was achieved for a small magnetically levitated steel ball [30]. This experiment was revived recently in [31] and [32]. The highest rotational speed of any macroscopic object was achieved in [33] by spinning graphene flakes at rotational speeds of up to 60 million rpm. However, in this paper, the physical experiments presented in [30]–[33] will not be considered in the comparison of electric drive systems as they have no possibility of driving an application.

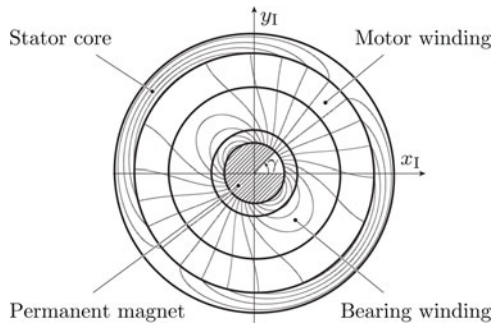

Fig. 1. Simplified machine cross section and definition of angular rotor position for a radially centered rotor. The magnetic flux lines of the diametrically magnetized permanent magnet (rotor pole-pair number $p_{\mathrm{pm}} = 1$) is shown.

A. Contributions and Outline of the Paper

In this paper, the control of a magnetically supported 500-krpm machine is presented, and measurement results are shown. The focus of this paper is the modeling of radial rotor dynamics, the design of the radial rotor position controller, and the closed-loop system control performance achieved by the implemented prototype in operation. The material in this paper was partially presented in [34] at the IEEE International Electric Machines & Drives Conference, Chicago, IL, USA, May 2013. The design of the implemented test bench and the power electronic actuators is presented in [7].

The machine prototype is designed for driving optical components such as mirrors in scanning applications. Due to the magnetic bearing, lifetimes of several thousand hours at speeds above $100\,\mathrm{krpm}$ can be achieved. Furthermore, it can be operated in high-purity or vacuum environments.

In Section II, the concept of the implemented machine prototype and the control algorithm is shown. The dynamics of the mechanical system are defined in Section III. The controller design is presented in Section IV. Finally, measurement results are shown in Section V, which verify the closed-loop system performance of the machine prototype in operation.

II. Integrated Bearing Design

The machine concept of the implemented prototype machine is based on a permanent-magnet synchronous machine presented in [1]. The magnetic bearing concept is proposed in [6]. Simplified machine cross sections are shown in Figs. 1 and 2. The machine topology features an integrated magnetic circuit for the generation of drive torque and radial bearing force as shown in Fig. 3. Therefore, the machine is considered as self-bearing.

The rotor construction and the choice of used materials are based on the results presented in [1]. As shown in Fig. 2, a titanium shaft in which three cylindrical permanent magnets are press fitted is used as rotor of the machine. The magnetic air gap between the rotor and the slotless amorphous-iron stator

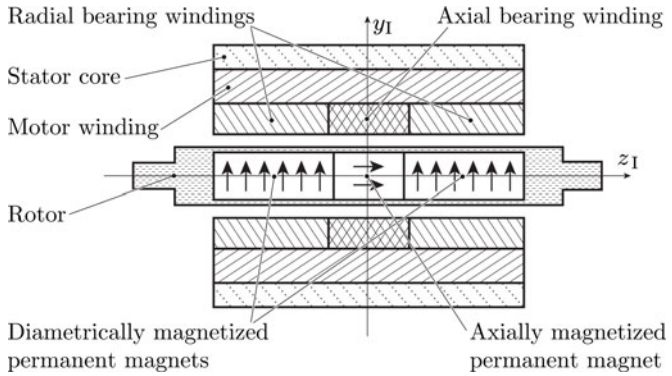

Fig. 2. Simplified machine cross section through the axis of rotation (not to scale). The rotor consists of a titanium shaft in which three cylindrical permanent magnets are press fitted. The magnetization direction of the permanent magnets is indicated by the arrows. A slotless amorphous-iron stack is used as stator core. The bearing windings and the motor winding are placed in the magnetic air gap between the rotor and the stator core.

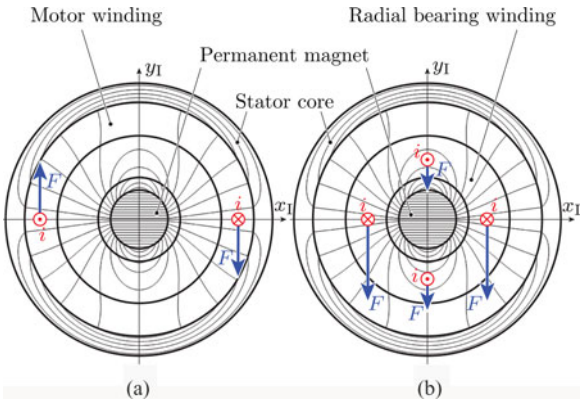

Fig. 3. Generation of drive torque and radial bearing force. (a) Generation of drive torque in the motor winding (pole-pair number $p_{\mathrm{w}} = 1$). (b) Generation of radial bearing force in a radial bearing winding ($p_{\mathrm{w}} = 2$). The magnetic flux lines of the diametrically magnetized permanent magnet (rotor pole-pair number $p_{\mathrm{pm}} = 1$) is shown. The winding currents i are perpendicular to the plane of drawing and the Lorentz forces F lie in the plane of drawing.

core is used to place a motor winding and a set of bearing windings. The magnetic field of the two diametrically magnetized permanent magnets is used for drive torque and radial bearing force generation as shown in Fig. 3. The magnetic field of the axially magnetized permanent magnet is used for the generation of axial bearing force.

Four important effects follow from the slotless construction of the windings and the ironless design of the rotor that distinguish the proposed design from reluctance-force-based AMB and are favorable for high-speed rotation.

1) In [7], it is verified experimentally that the design features *linear* force/torque-to-winding current relationships.
2) In contrast to reluctance-force-based AMB, the proposed bearing actuators are based on Lorentz force, i.e., the achievable actuator bandwidth is not limited by eddy currents in the rotor iron [7].

TABLE I
MECHANICAL PROPERTIES OF THE IMPLEMENTED MACHINE PROTOTYPE

Symbol	Quantity	Value
n_{max}	Maximum rotational speed	$500\,000\,\mathrm{rpm}$
P_{motor}	Rated machine power	$300\,\mathrm{W}$ [7]
m	Rotor mass	$12.3\,\mathrm{g}$
L_{rotor}	Rotor length	$55\,\mathrm{mm}$
D_{rotor}	Rotor diameter	$7.3\,\mathrm{mm}$
x_{max}	Maximum rotor displacement	$0.25\,\mathrm{mm}$
I_{x_0}	Inertia about x_0-axis	$2.07 \times 10^{-6}\ \mathrm{kg \cdot m^2}$
I_{z_0}	Inertia about z_0-axis	$71.5 \times 10^{-9}\ \mathrm{kg \cdot m^2}$
k_α	Magnetic stiffness	$-0.029\ N \cdot \mathrm{m/rad}$
$k_{x_{\mathrm{I}}}$	Magnetic stiffness	$-342\,\mathrm{N/m}$
χ_{pm}	Radial bearing constant	$71.6 \times 10^{-3}\ \mathrm{N/A}$

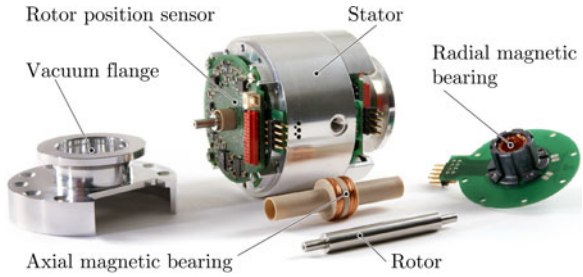

Fig. 4. Photo of the implemented self-bearing machine prototype with dismantled rotor, axial, and radial magnetic bearing.

3) Simulations have shown that the rotor eddy-current losses caused by the magnetic field of the bearing windings are negligible.
4) The resulting winding inductances are small compared to slotted designs. Therefore, the bearing currents can be controlled with low reactive power consumption, and low-voltage power electronics using ultrafast switching frequencies [7]. As a consequence, high bearing actuator bandwidths can be achieved [7].

The mechanical data of the implemented machine prototype are given in Table I , and a picture of the implemented machine with dismantled magnetic bearing is shown in Fig. 4 . The mechanical, electromagnetic, and thermal design of the machine is beyond the scope of this paper. The interested reader is referred to [7] for a more detailed description of the design procedure and the derivation of rated machine power (see Table I).

A. Radial Bearing Force Generation

The radial bearing forces are generated in two star-connected three-phase skewed air-gap windings with a pole-pair number $p_{\mathrm{w}} = 2$. The winding phase currents are denoted with i_{A}, i_{B}, and i_{C}. The interested reader is referred to [35] for a detailed description of the used winding type. Due to the heteropolar field of the permanent magnet (cf., Fig. 3), the winding currents have to be controlled by a field-oriented control algorithm [6]. In [7] and [35], it was analytically derived and experimentally verified that the proposed design features linear force/torque-to-winding current relationships. According to [7], the radial

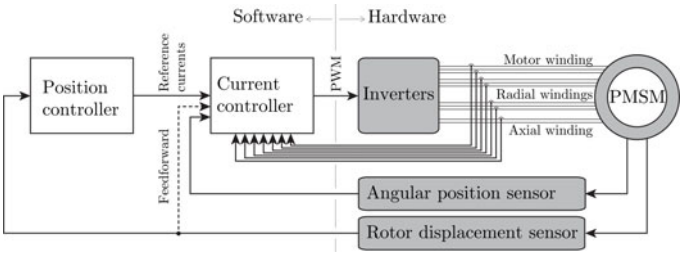

Fig. 5. Control block diagram of the self-bearing machine. The rotor position is controlled in an outer control loop, whereas the reference winding currents are tracked in an inner control loop.

bearing force vector

$$\boldsymbol{F} = \begin{bmatrix} F_{x_\mathrm{I}} \\ F_{y_\mathrm{I}} \\ F_{z_\mathrm{I}} \end{bmatrix} = \frac{3}{2}\chi_{\mathrm{pm}} \begin{bmatrix} i_d \\ i_q \\ 0 \end{bmatrix} \tag{1}$$

can be calculated as a function of winding currents i_d and i_q. As defined in [7], the currents are defined in field-oriented coordinates. The force vector $\boldsymbol{F}$ is expressed in stator-fixed Cartesian coordinates with principal axes $(x_\mathrm{I}, y_\mathrm{I}, z_\mathrm{I})$. The mathematical bearing model and the calculation of the bearing constant χ_{pm} are given in [7].

B. Rotor Position Control

The rotor is levitated by controlling the rotor position by means of feedback control. A printed-circuit-board-based position sensor system, as shown in Fig. 4, is implemented for measuring the rotor position in the feedback path of the control scheme. The radial rotor position measurement is based on eddy-current sensors presented in [36], whereas the axial and the angular positions are obtained by Hall-effect-based stray field measurements [7].

A cascaded control scheme shown in Fig. 5, as proposed in [7], is used for the control of the rotor position. Radial and axial rotor displacements are measured and controlled in an outer control loop. The output of the rotor position controller is a set of reference winding currents, which are then tracked in a field-oriented inner control loop. Thus, a measurement of the angular rotor position γ (cf., Fig. 1), given by the trigonometric terms $\cos(\gamma)$ and $\sin(\gamma)$, has to be obtained from the angular position sensor. The implemented bearing power electronics and the achieved control performance of the current control loop are presented in [7].

Following the rule of thumb for cascaded control systems stated in [37], the controller gains are chosen such that the current control loop will not affect the rotor position control loop. In the presented control scheme, the response time of the current control loop is more than ten times faster than the response time of the rotor position control loop. Therefore, the effects of the current control loop are neglected for the design of the rotor position control loop. The accuracy of this simplification is verified in Section V. by closed-loop system measurements.

In the proposed slotless bearing concept, all six DOFs of the rotor are actively controlled by Lorentz forces. In contrast to reluctance-force-based actuators, the proposed design features *linear* force-to-current relationships [7]. Hence, centralized *linear* multivariable state feedback control can be applied directly without linearization of bearing actuators.

The advantage of controlling all six DOFs of the rotor actively is that all rigid-body modes including nutation and precession can be controlled by the position controller. The disadvantage when compared to designs that use a passive stabilization of some DOF (e.g., [15]) is that the system complexity is higher in the present design.

C. Challenges and Limitations

The biggest challenge for the control of the bearing is the fact that the radial bearing currents have to be controlled by a field-oriented control algorithm up to a rotational frequency of 8.33 kHz (500 krpm$/$(60 s/min)). Phase errors in the angular transformations result in wrong radial bearing force *directions* [cf., (1)]. Therefore, an undesired cross coupling between the axes of the rotor position controller will be caused by the false controller inputs. This coupling will inevitably result in a severe degradation of the overall controller performance or even cause instability.

Another challenge for the bearing control is the gyroscopic couplings between the axes of the radial bearing controller which increase with the rotational speed [13]. Furthermore, the nutation mode frequency increases with the rotational speed [13]. In the proposed design, the nutation mode has to be actively controlled by the magnetic bearing to achieve satisfactory control performance. Therefore, high-bandwidth bearing actuators and control are necessary to stabilize the system.

The proposed machine design relies mainly on Lorentz forces for bearing force generation. Thus, the load capacity of the magnetic bearing that can be achieved is small compared to reluctance-force-based AMB systems. In the presented optical application, this limitation is not relevant. However, if the proposed machine topology is applied to applications with higher bearing loads, this limitation might be relevant.

A bending of the rotor cannot be actively damped. Therefore, the machine has to be operated below the bending mode frequency. Hence, the maximum rotational speed is limited by the mechanical design and dynamics of the rotor.

The implemented prototype is designed for driving mirrors in laser scanning applications. Therefore, the absolute rotational speed of the rotor is maximized in the design process to maximize the rotational speed and the repetition frequency of the laser beam [7]. The main difficulty of maximizing the absolute rotational speed rather than the surface speed is the increasing high frequency losses which are a function of the absolute rotational speed (e.g., the rotor iron losses in reluctance-force-based AMB). In the case of self-bearing motors, additional difficulties arise from the high rotational frequency of the coordinate transformations in the field-oriented current control algorithms as stated earlier. The presented prototype is designed for a maximum rotational speed of 500 krpm. This is equivalent to a surface speed of 191 m/s in the active part of the rotor or a DN number of 3.65 million DN ($\mathrm{mm{\cdot}rpm}$). To the authors'

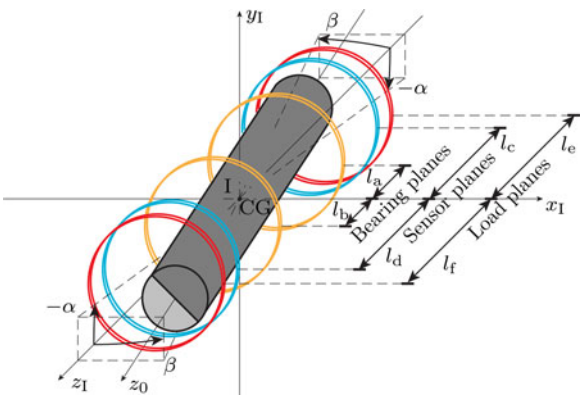

Fig. 6. Schematic of the rigid rotor geometry and coordinate definitions.

knowledge, this is the highest absolute rotational speed achieved by magnetically levitated electrical drive systems so far. However, there are state-of-the-art designs that feature higher DN numbers (e.g., [38]).

III. Rotor Dynamics Modeling

This section briefly describes the dynamics of the mechanical system within the AMB control loop. In Section A, the dynamics of a rigid rotor are given. These dynamics are the basis for the design of the rotor position estimator and controller presented in Section IV. An extended rotor dynamics model accounting for the flexible structure of the rotor is presented in Section B. Both rotor dynamic models will be compared to each other in Section V.

A. Dynamics of the Rigid Rotor

A schematic of the rotor geometry is shown in Fig. 6. A stator-fixed coordinate system I with principal axes $(x_\mathrm{I}, y_\mathrm{I}, z_\mathrm{I})$ and a rotor-fixed coordinate system CG is introduced. The origin of CG is defined as the center of mass of the rotor. The principal axes of CG (x_0, y_0, z_0) coincide with the principal axes of inertia. The rotor position can be described by the position of CG with respect to I, defined by the transversal displacement $(x_\mathrm{CG}, y_\mathrm{CG}, z_\mathrm{CG})$ and the Cardan angles (α, β, γ).

The definition of radial state dynamics is based on the assumption 1) that the rotor is symmetric and rigid, and 2) that the deviations of the principal axes of I and CG are small compared to the rotor dimensions. Due to assumption 2, linearization is applicable, which yields that α and β can be characterized as inclinations about the x_I- and y_I-axis [13].

The equations of motion for the radial state vector

$$\boldsymbol{z} = [\,\beta \quad x_\mathrm{CG} \quad -\alpha \quad y_\mathrm{CG}\,]^T \tag{2}$$

can be derived from Lagranges's equations [13]. For a constant angular frequency $\Omega = \frac{\partial \gamma}{\partial t}$ and given the assumptions 1 and 2, the equations of motion can be written in the linearized form [13]

$$M\ddot{\boldsymbol{z}} + G(\Omega)\dot{\boldsymbol{z}} + S\boldsymbol{z} = V\boldsymbol{u} + \boldsymbol{g} + W\boldsymbol{f}_\mathrm{load} \tag{3}$$

where the dot denotes the derivative with respect to time, $\dot{\boldsymbol{z}} = \frac{\partial \boldsymbol{z}}{\partial t}$. Even though a constant Ω is assumed, the dynamics (2) can be used as an approximation when Ω varies only slowly when compared to the radial dynamics, i.e., when $\dot{\Omega}$ is negligible. The diagonal mass matrix

$$M = \mathrm{diag}\,(I_{y_0}, m, I_{x_0}, m) \tag{4}$$

and the gyroscopic coupling matrix

$$G(\Omega) = I_{z_0}\,\Omega \begin{bmatrix} 0 & 0 & 1 & 0 \\ 0 & 0 & 0 & 0 \\ -1 & 0 & 0 & 0 \\ 0 & 0 & 0 & 0 \end{bmatrix} \tag{5}$$

are defined according to [13]. m denotes the rotor mass and I_{x_0}, I_{y_0}, and I_{z_0} the inertia of the rotor about the x_0-, y_0-, and z_0-axis. Given the symmetry of the rotor, $I_{x_0} = I_{y_0}$ can be assumed. The magnetic stiffness, resulting from the high-permeability stator core, is generally a nonlinear function of the rotor displacements. It was shown in [6] that for the presented type of machines this force can be approximated by a linear rotor displacement dependent destabilizing force. Therefore, the linear negative stiffness of the configuration is defined by the matrix

$$S = \mathrm{diag}\,(k_\alpha, k_{x_\mathrm{I}}, k_\alpha, k_{x_\mathrm{I}}) \tag{6}$$

with the stiffness constants $k_\alpha = -\partial T_{x_\mathrm{I}}/\partial\alpha$ and $k_{x_\mathrm{I}} = -\partial F_{x_\mathrm{I}}/\partial x_\mathrm{CG}$. The generalized forces on the right-hand side of (3) consist of all external forces acting on the rotor, such as the force caused by the magnetic bearing current vector

$$\boldsymbol{u} = [\,i_{d,\mathrm{B1}} \quad i_{q,\mathrm{B1}} \quad i_{d,\mathrm{B2}} \quad i_{q,\mathrm{B2}}\,]^T \tag{7}$$

a known load force (e.g., the force of gravity caused by the rotor mass)

$$\boldsymbol{g} = [\,T_{y_\mathrm{I},\mathrm{ff}} \quad F_{x_\mathrm{I},\mathrm{ff}} \quad -T_{x_\mathrm{I},\mathrm{ff}} \quad F_{y_\mathrm{I},\mathrm{ff}}\,]^T \tag{8}$$

and a force component resulting from an unknown load force

$$\boldsymbol{f}_\mathrm{load} = [\,F_{x_\mathrm{I},\mathrm{e}} \quad F_{y_\mathrm{I},\mathrm{e}} \quad F_{x_\mathrm{I},\mathrm{f}} \quad F_{y_\mathrm{I},\mathrm{f}}\,]^T\,. \tag{9}$$

The components of $\boldsymbol{f}_\mathrm{load}$ act on the two load planes defined in Fig. 6. The transformation of $\boldsymbol{f}_\mathrm{load}$ and $\boldsymbol{u}$ into center of mass coordinates is done with the matrices

$$W = \begin{bmatrix} -l_\mathrm{e} & 0 & l_\mathrm{f} & 0 \\ 1 & 0 & 1 & 0 \\ 0 & -l_\mathrm{e} & 0 & l_\mathrm{f} \\ 0 & 1 & 0 & 1 \end{bmatrix} \tag{10}$$

$$V = \frac{3}{2}\chi_\mathrm{pm} \begin{bmatrix} -l_\mathrm{a} & 0 & l_\mathrm{b} & 0 \\ 1 & 0 & 1 & 0 \\ 0 & -l_\mathrm{a} & 0 & l_\mathrm{b} \\ 0 & 1 & 0 & 1 \end{bmatrix}. \tag{11}$$

Radial displacements of the rotor can be measured at the sensor planes (cf., Fig. 6) with the embedded eddy-current sensor, yielding the vector

$$\boldsymbol{y}_\mathrm{sens} = \begin{bmatrix} x_\mathrm{c} \\ y_\mathrm{c} \\ x_\mathrm{d} \\ y_\mathrm{d} \end{bmatrix} = \begin{bmatrix} -l_\mathrm{c} & 1 & 0 & 0 \\ 0 & 0 & -l_\mathrm{c} & 1 \\ l_\mathrm{d} & 1 & 0 & 0 \\ 0 & 0 & l_\mathrm{d} & 1 \end{bmatrix} \boldsymbol{z} \tag{12}$$

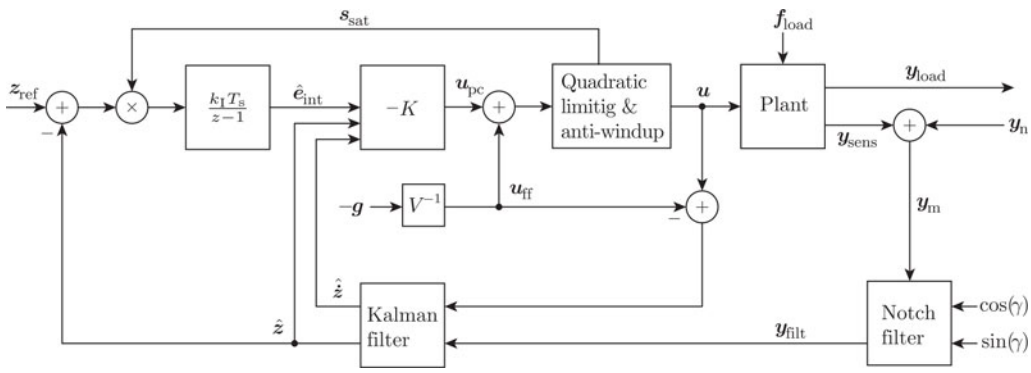

Fig. 7. Proposed multivariable feedback control scheme for the radial rotor position. An LQG controller with integral action and quadratic control input limiting is implemented.

or by means of external position sensor at the load planes yielding the vector

$$\boldsymbol{y}_{\mathrm{load}} = \begin{bmatrix} x_{\mathrm{e}} \\ y_{\mathrm{e}} \\ x_{\mathrm{f}} \\ y_{\mathrm{f}} \end{bmatrix} = \begin{bmatrix} -l_{\mathrm{e}} & 1 & 0 & 0 \\ 0 & 0 & -l_{\mathrm{e}} & 1 \\ l_{\mathrm{f}} & 1 & 0 & 0 \\ 0 & 0 & l_{\mathrm{f}} & 1 \end{bmatrix} \boldsymbol{z}. \tag{13}$$

B. Dynamics of the Flexible Rotor

The rotor dynamics presented in the previous section assume a rigid rotor structure. Thus, possible bending of the rotor is neglected. In order to understand the dynamics including bending effects, a model of the flexible rotor, based on the well-known Euler Bernoulli beam theory [39], is introduced. The model is implemented in state-space representation according to the procedure described in [13].

Calculated transfer functions based on this accurate system model will be validated against measurements in Section V.

IV. Radial Rotor Position Controller Design

In contrast to most other magnetic bearing concepts, the *linear* bearing force-to-current relationship of the proposed design improves the achievable accuracy of system dynamics modeling. Furthermore, the slotless design of the windings enables controlling bearing forces up to high bandwidths [7].

The dynamics (3) describe a nonlinear, multivariable system. The nonlinearity is a result of the gyroscopic effect, which is a function of the time-varying angular frequency Ω. However, provided that Ω varies only slowly when compared to the radial dynamics, the system behavior is considered as a switched linear system [40]. Thus, for a constant Ω, optimal control algorithms such as $\mathcal{H}_\infty$ or LQG can be applied.

The implemented MIMO linear state feedback control scheme is shown in Fig. 7. In order to enable a computationally efficient and simple real-time implementation of the control algorithm, an LQR and a Kalman filter based on (3), for $\Omega = 0$, is evaluated, i.e., (time-varying) gyroscopic couplings are neglected by the control algorithm. This controller can be implemented very efficiently, in a straight-forward way, using a single set of controller and state estimator matrices over the whole speed range. The closed-loop system performance, including the model error caused by the neglected gyroscopic couplings, is analyzed in Section V.

Generally, the use of magnetic bearings enables changing the characteristics of the bearing system during operation [13]. In many applications, this is a desirable or necessary key feature of the AMB system. Also, in the present application this can be achieved easily by changing the controller parameters during operation. However, it will be shown that the implemented position controller is robust enough to allow operating the prototype machine over the whole speed range with a single set of controller parameters. Therefore, the simplicity of a control scheme using a single set of controller parameters was preferred over more complex implementations. In other applications with higher gyroscopic couplings (e.g., flywheels), this simplification is generally not possible, and an adaptation of controller parameters is required.

The known load force $\boldsymbol{g}$ is fed forward in the controller scheme. The controller is implemented on a signal processor for discrete time steps k. In the following sections, a short description of state estimation and feedback controller design is given. The interested reader is referred to [27] and [37] for a detailed description of the procedures.

A. State Estimation

Since states like radial rotor velocities cannot be measured directly with the employed position sensors, and to enable noise rejection, a Kalman filter of the form

$$\begin{aligned} \begin{bmatrix} \hat{\boldsymbol{z}}(k|k) \\ \hat{\dot{\boldsymbol{z}}}(k|k) \end{bmatrix} &= N_{\mathrm{K}} \begin{bmatrix} \hat{\boldsymbol{z}}(k-1|k-1) \\ \hat{\dot{\boldsymbol{z}}}(k-1|k-1) \end{bmatrix} \\ &\quad + O_{\mathrm{K}} \left(\boldsymbol{u}(k-1) - \boldsymbol{u}_{\mathrm{ff}}(k-1) \right) \\ &\quad + M_{\mathrm{K}}\, \boldsymbol{y}_{\mathrm{filt}}(k) \end{aligned} \tag{14}$$

based on the dynamics (3) is implemented. Here, $\hat{\boldsymbol{z}}(k_1|k_0)$ denotes an estimate of $\boldsymbol{z}$ at time k_1 with knowledge up to time k_0. In order to enable state estimation which is independent of known load force $\boldsymbol{g}$, the feedforward control input $\boldsymbol{u}_{\mathrm{ff}}(k-1)$ is subtracted from the actual control input $\boldsymbol{u}(k-1)$.

Then, the calculation of the filter gain matrices N_{K}, O_{K}, and M_{K} is performed according to [37]. The design is based on the assumption that the measured rotor position $\boldsymbol{y}_{\mathrm{sens}}$ is disturbed

by an additive zero-mean white Gaussian noise signal $\boldsymbol{y}_{\mathrm{n}}$ with known covariance matrix. The process noise is defined by the unknown load force vector $\boldsymbol{f}_{\mathrm{load}}$, which is also assumed to be zero-mean white Gaussian noise with known covariance matrix.

B. Linear State Feedback Controller

An LQR of the form

$$\boldsymbol{u}_{\mathrm{pc}}(k) = -K \begin{bmatrix} \hat{\boldsymbol{e}}_{\mathrm{int}}(k|k) \\ \hat{\boldsymbol{z}}(k|k) \\ \hat{\dot{\boldsymbol{z}}}(k|k) \end{bmatrix} \tag{15}$$

is implemented. In order to enable offset-free controller performance, the state vector is augmented with an integral of the control error $\boldsymbol{z}_{\mathrm{ref}} - \hat{\boldsymbol{z}}$ with respect to time, denoted with $\hat{\boldsymbol{e}}_{\mathrm{int}}$. Typically, the reference rotor position is set to the geometric center of the machine, $\boldsymbol{z}_{\mathrm{ref}} = \boldsymbol{0}$.

The calculation of controller matrix K is based on a weighted integral quadratic cost function [37]. The weighting factors for the cost function are chosen such that the required closed-loop system performance is met. The choice of the weights determines the stiffness of the magnetic bearing. Furthermore, the frequency of the rigid body-modes can be set to values that do not conflict with the rotational frequency.

Due to the LQR structure, the task of controller tuning is therefore reduced to choosing the weights of a single cost function. The outcome of this is a significant simplification in practice when compared to PID-based control, where typically different controllers are used for different states of the MIMO system.

C. Quadratic Controller Output Limiting and Antiwindup

Overheating of the bearing windings can be avoided by limiting the total power loss in the windings. The power loss consists of proximity losses, which are mainly caused by the permanent magnet flux density, and winding current conduction losses, which are proportional to $i_d^2 + i_q^2$ [7]. In the presented prototype, the conduction losses are the dominant loss component. Therefore, only the conduction losses are limited by the controller. Thus, a quadratic limiting function

$$\boldsymbol{u}(k) = \Lambda(k)\left(\boldsymbol{u}_{\mathrm{pc}}(k) + \boldsymbol{u}_{\mathrm{ff}}(k)\right) \tag{16}$$

with the scaling variables

$$\Lambda(k) = \mathrm{diag}\left(\lambda_1(k), \lambda_1(k), \lambda_2(k), \lambda_2(k)\right) \tag{17}$$

$$\lambda_1^2(k) = \min\left\{1, \frac{i_{\max}^2}{i_{d,\mathrm{B1}}^2(k) + i_{q,\mathrm{B1}}^2(k)}\right\} \tag{18}$$

$$\lambda_2^2(k) = \min\left\{1, \frac{i_{\max}^2}{i_{d,\mathrm{B2}}^2(k) + i_{q,\mathrm{B2}}^2(k)}\right\} \tag{19}$$

is proposed, limiting the amplitude of the phase currents to $i_{\max}$ but preserving the angular direction of the bearing force. Both i_d and i_q are scaled with the same factor such that $i_d^2 + i_q^2 \leq i_{\max}^2$. The limiting is performed for each of the two bearing windings individually. When any of the two bearing windings is in saturation, the integration of the control error is disabled by the control signal $\boldsymbol{s}_{\mathrm{sat}}$ to prevent integrator windup.

D. Unbalance Force Rejection Control

So far, rotor displacements caused by unbalance were not considered. When accelerating the rotational frequency through the critical frequencies of the rigid-body rotor system, the axis of rotation will shift from its axis of geometry to the axis of inertia [13]. These axes might differ from each other due to unbalance [13]. During the acceleration of the presented prototype, the eigenfrequencies of the *forward whirling pendulous vibration* are passed at 9.4 krpm and of the *nutation* at 11.1 krpm.

The basic idea of unbalance force rejection control is to reduce the bearing loss by suppressing the magnetic bearing control input for unbalance caused rotor displacements [13], [41], [42]. This allows the rotor rotating around its axis of inertia. In the presented control scheme, this is done by suppressing the sensor signals synchronous to Ω, for rotational frequencies above the rigid-body critical frequencies. A narrow band-stop filter at the (time-varying) angular frequency Ω for the position measurement is implemented. The filter is based on the generalized notch filter proposed in [41]. The fact, that a notch-filtered position signal is used for state estimation might affect the closed-loop stability, when the machine is rotating close to a critical frequency of the bearing system. Therefore, the notch filter is only enabled for speeds above the rigid-body critical frequencies (i.e., for rotational speeds above 60 krpm).

V. Results

The presented control scheme is implemented on an Altera NIOS II signal processor with a controller execution frequency of 33.3 kHz. The achieved controller performance is analyzed in Section A. Due to the instability of the open-loop system, the verification of the presented system modeling is done by a set of measured closed-loop system transfer functions in Section B. Finally, measurement results are shown in Section C. for 500 krpm.

A. Closed-Loop System Performance

A *Campbell diagram* of the closed-loop system is shown in Fig. 8. The eigenfrequencies of the closed-loop system are plotted for varying rotational speed. At 500 krpm, the *nutation* frequency is 575 Hz, the *pendulous vibration* frequency 156 Hz, and the *precession* frequency 81 Hz. Furthermore, it can be seen that the machine was designed such that the bending mode frequencies are higher than the maximum rotational frequency of 8.33 kHz at 500 krpm. Therefore, it can be assured that the bending resonances are not excited by the unbalance of the rotor [13].

The performance of the controller is analyzed in the frequency domain by the gain of the closed-loop system, shown in Fig. 7. The input of the system is defined as force vector $\boldsymbol{f}_{\mathrm{load}}$, and the output as rotor displacement vector $\boldsymbol{y}_{\mathrm{load}}$. Single input-to-output transfer functions are a poor performance measurement of a MIMO system, as the gain might vary drastically depending on the direction of the input vector [37]. Therefore, the singular value decomposition is used to analyze the performance of the

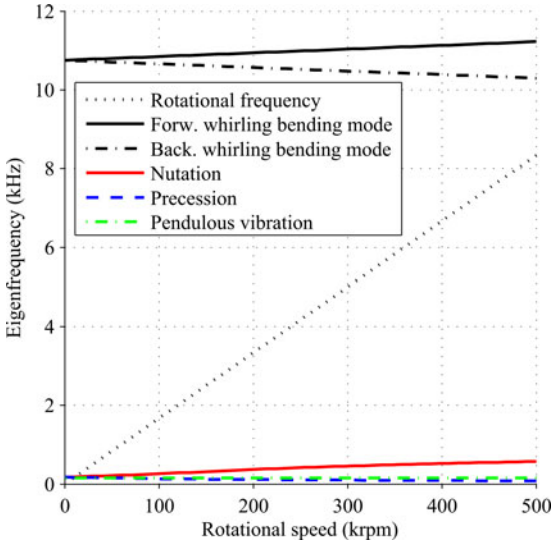

Fig. 8. Campbell diagram for the rated speed range. The eigenfrequencies of the closed-loop system are calculated based on the flexible rotor model system dynamics.

system. The system disturbance is defined as

$$\boldsymbol{f}_{\mathrm{load}} = \frac{F_{\mathrm{dist}}}{\sqrt{2}} \begin{bmatrix} \cos(\omega t) \\ h_{\mathrm{dir}} \sin(\omega t) \\ h_{\mathrm{mode}} \cos(\omega t) \\ h_{\mathrm{dir}}\, h_{\mathrm{mode}} \sin(\omega t) \end{bmatrix} \tag{20}$$

with ω being the angular frequency of the disturbance, F_{dist} the Euclidean norm of the disturbance vector and t the time. The singular-value input directions of $\boldsymbol{f}_{\mathrm{load}}$ are defined as *forward* ($h_{\mathrm{dir}} = 1$) and *backward* ($h_{\mathrm{dir}} = -1$) rotating *parallel* ($h_{\mathrm{mode}} = 1$) and *conical* ($h_{\mathrm{mode}} = -1$) disturbances. Similarly, the output directions of $\boldsymbol{y}_{\mathrm{load}}$ are *forward* and *backward* rotating *parallel* and *conical* whirls. Given the symmetry of the machine, it can be seen that the direction of the input is the same as the direction of the output. Therefore, the performance can be analyzed by a set of four singular-value transfer functions.

In Figs. 9 and 10, singular-value transfer functions are shown using *rigid* and *flexible* rotor model system dynamics. Both models are calculated for the maximum rotational speed of 500 krpm. In both plots, exactly the same feedback controller is used to stabilize the system. All transfer functions are given for the system having the notch filter disabled. It can be seen that both models yield the same results for all rigid-body modes, which have an eigenfrequency below 1 kHz (cf., Fig. 8). In the proposed machine design, all bending modes of the rotor are stable. Therefore, only the rigid-body modes have to be actively controlled by the magnetic bearing. Thus, it can be concluded that it is reasonable to use rigid-body rotor dynamics for the design of the rotor position controller.

In Fig. 10, it can be seen that the transfer functions for *conical* disturbances feature peak values at the nutation (575 Hz) and the precession (81 Hz) frequencies. These peaks are undesirable, but they are unavoidable for real systems [37]. The peak values could be further reduced by including the (time-varying) gyroscopic couplings in the controller design. Nevertheless, it can be concluded from the simulations that the controller yields

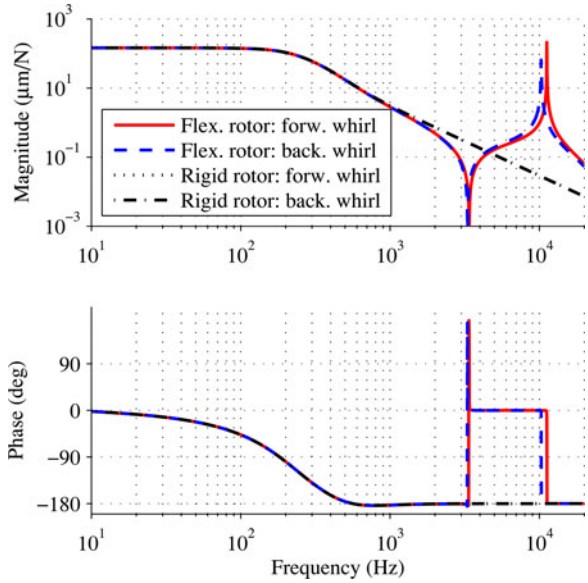

Fig. 9. Calculated closed-loop singular-value transfer functions for forward and backward rotating *parallel* disturbances (f_{load}) to resulting *parallel* whirls ($\boldsymbol{y}_{\mathrm{load}}$) for a rotational speed of 500 krpm. Values are given for two systems using the same feedback controller but different rotor dynamics modeling. Both curves using the rigid rotor model (forward and backward whirl) coincide. Therefore, only one curve can be seen in the plot.

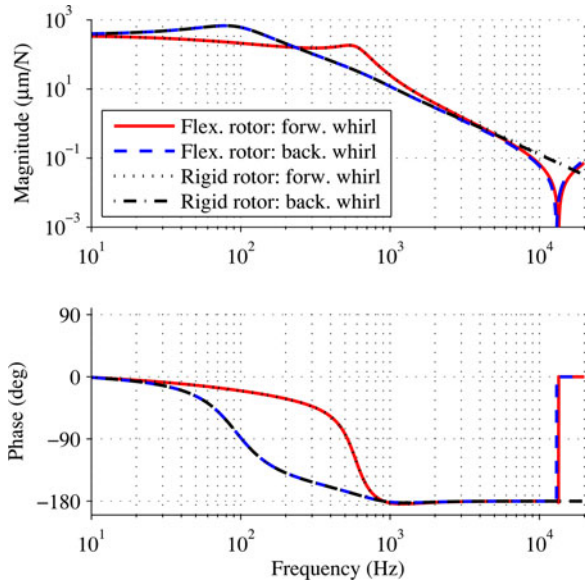

Fig. 10. Calculated closed-loop singular-value transfer functions for forward and backward rotating *conical* disturbances (f_{load}) to resulting *conical* whirls (y_{load}) for a rotational speed of 500 krpm. Values are given for two systems using the same feedback controller but different rotor dynamics modeling. Peak values can be observed at the *precession* (backward whirl at 81 Hz) and the *nutation* (forward whirl at 575 Hz) mode frequency.

sufficient performance to stabilize the mechanical system, and it is robust enough to operate the machine over the whole speed range with a single set of controller parameters.

B. Measured Singular-Value Transfer Functions

The presented system modeling is verified by a set of measured singular-value transfer functions. The measurements are performed on the machine during operation at a rotational speed

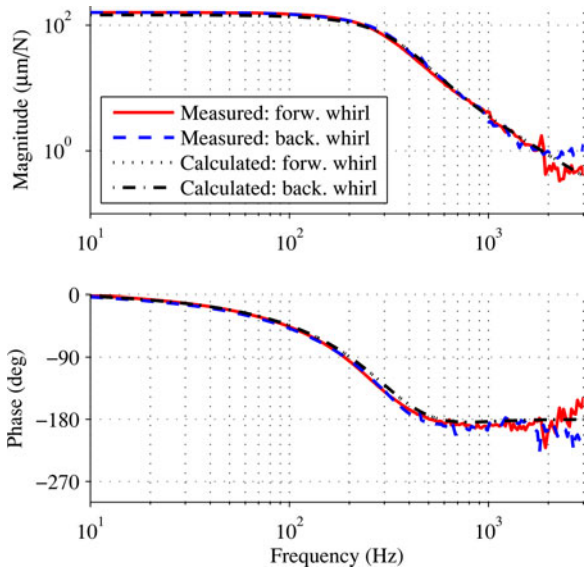

Fig. 11. System model verification: Measured and calculated closed-loop singular-value transfer functions for forward and backward rotating *parallel* disturbances to resulting *parallel* whirls, for a rotational speed of 240 krpm.

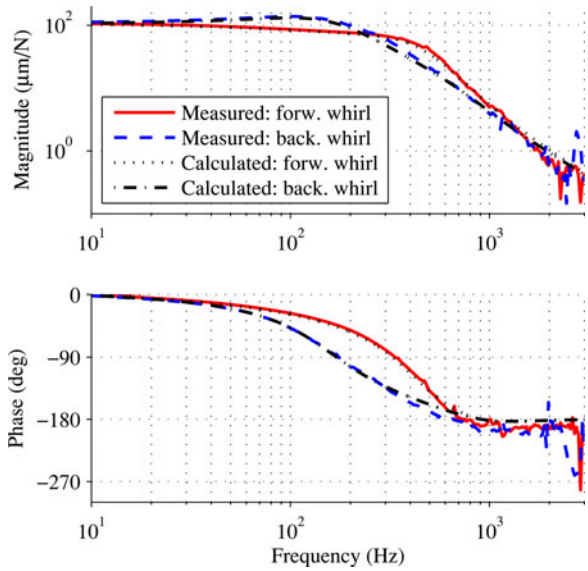

Fig. 12. System model verification: Measured and calculated closed-loop singular-value transfer functions for forward and backward rotating *conical* disturbances to resulting *conical* whirls, for a rotational speed of 240 krpm. A measurement of the resulting backward whirl at the *precession* mode frequency is shown at 160 Hz. Similarly, a measurement of the resulting forward whirl at the *nutation* mode frequency is shown at 340 Hz.

of 240 krpm ($\Omega = 2\pi{\cdot}4$ kHz). The rotor is disturbed by means of applying sinusoidal radial forces with the magnetic bearing. The resulting whirls are detected by the displacement vector $\boldsymbol{y}_{\mathrm{sens}}$. A measurement of the closed-loop system transfer function can then be obtained by the orthogonal correlation method described in [43]. Because the rotor is disturbed by a considerable radial force during the measurement, the rotational speed is limited to 240 krpm during the measurement due to safety reasons. Although the presented results verify only the system modeling at 240 krpm, they still demonstrate the accuracy of the presented system modeling.

In Figs. 11 and 12, the results for forward and backward rotating *parallel* and *conical* disturbances are given and compared to calculated values. The calculation of the transfer functions is based on the mechanical dimensions and properties of the rotor system and was not adjusted or fitted to any measurement. The measured transfer functions correspond well with the calculated ones up to a frequency of roughly 2 kHz. At this frequency, the implemented measurement method reaches its limitations. For higher frequencies, the transfer function cannot be measured accurately because the resulting rotor displacements are significantly smaller than the rotor position measurement noise. From the remarkable accordance of calculated and measured transfer functions, it can be concluded that the presented system modeling is accurate. Furthermore, it can be concluded that the cascaded control structure is applied successfully, meaning that the performance of the rotor position control loop is not affected by the current control loop.

C. Closed-Loop System Measurement at 500 krpm

Fig. 13 shows a measurement of the machine in operation at a rotational speed of 500 krpm. Due to the low sampling frequency of the employed eddy-current sensors of 33.3 kHz, the measurement of the radial rotor tip displacement x_{e} [cf., (13)] is obtained by an external (1-D) ultrahigh-speed optical displacement sensor (Keyence LK-H022) with a sampling frequency of 100 kHz. An Ω-synchronous displacement of about ± 17 µm can be observed. Furthermore, measurements show that these displacements increase with the rotational speed. At 500 krpm, Ω

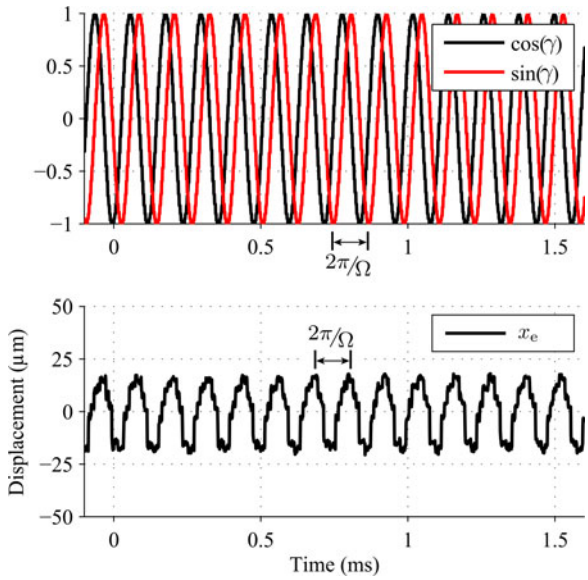

Fig. 13. Closed-loop system measurement of the machine in operation at a rotational speed of 500 krpm. The upper plot shows the Hall-effect-based angular position measurement to verify the actual rotational speed. A measurement of the radial rotor tip displacement x_{e} is shown in the lower plot. The period of a single rotation ($2\pi/\Omega$) is marked in both plots.

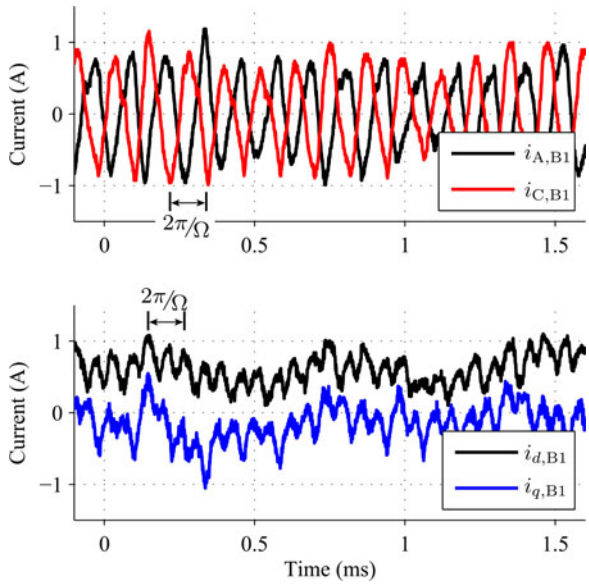

Fig. 14. Measured bearing winding currents for the 500-krpm measurement shown in Fig. 13. The measured phase currents $i_{\mathrm{A,B1}}$ and $i_{\mathrm{C,B1}}$ of the first (star-connected three-phase) radial bearing winding (B1) are given in the upper and their transformation into field-oriented dq-coordinates in the lower plot. The definition of the currents can be found in Section A. The period of a single rotation ($2\pi/\Omega$) is marked in both plots.

is far beyond the bandwidth of the rigid mechanical system (cf., Fig. 8). From this, it can be concluded that the displacements are partly caused by a deformation of the rotor. Due to the high rotational frequency and the quadratic scaling of the unbalance excitation with the rotational frequency [13], it is believed that most of the deformation is caused by the unbalance. Due to the small frequency gap between the rotational frequency and the bending mode frequency, even small unbalances cause deformations in the micrometer range. A possible rotor deformation can be seen in the modal analysis presented in [7]. The unbalance caused deformations can be reduced by balancing the rotor in multiple axial planes at the maximum rotational speed.

The bearing winding phase currents and their transformation into field-oriented currents $i_{d,\mathrm{B1}}$ and $i_{q,\mathrm{B1}}$ are shown in Fig. 14, for the measurement shown in Fig. 13. The transformation is done by an amplitude invariant Park transformation, using the measurement of the angular rotor position as transformation angle. The currents $i_{d,\mathrm{B1}}$ and $i_{q,\mathrm{B1}}$ are two of the inputs which are manipulated by the controller. According to (1), they are proportional to the bearing forces in x_{I}- and y_{I}-direction. It can be seen from Fig. 14, that the bearing currents exhibit no Ω-synchronous component, but a component synchronous to $2\,\Omega$. Thus, the suppression of Ω-synchronous rotor displacements, by the notch filter, is applied successfully. The component synchronous to $2\,\Omega$ follows from a second harmonic in the position measurement and is therefore not suppressed. The bearing losses could be further reduced by suppressing also the second-harmonic component of the rotational frequency from the measured position signals.

The maximum speed of the current prototype is not limited by the magnetic bearing but by the mechanical construction of the rotor [44]. Thus, a higher speed could be achieved with a scaled-down version of the prototype [44].

VI. Conclusion

The machine prototype presented in this paper overcomes several limitations of previously presented high-speed magnetically levitated electrical drive systems. Both, motor and bearing windings are implemented as air-gap windings. Thus, the design features linear bearing force-to-current relationships [7], improving the accuracy of the system dynamics modeling considerably. Furthermore, the slotless design of the bearing windings enables achieving very high actuator bandwidths [7]. The presented linear dynamics of the mechanical system are verified by singular-value transfer function measurements. A multivariable state feedback control algorithm based on LQG control is proposed. The implemented Kalman filter yields sufficient noise rejection to operate the machine and enables to obtain estimates of the nonmeasurable system states. The control algorithm proved to perform well in practice, stabilizing the system over the design speed range of the high-speed machine with a single set of controller parameters. Closed-loop system measurements of the machine, rotating at $500\,\mathrm{krpm}$, verify the functionality of the overall system and prove the feasibility of the proposed control.

Acknowledgment

The authors would like to thank Dr. C. Zwyssig from Celeroton AG and Dr. P. Buhler from Mecos AG for their technical advice.

References

[1] J. Luomi, C. Zwyssig, A. Looser, and J. W. Kolar, "Efficiency optimization of a 100-W 500 000-r/min permanent-magnet machine including air-friction losses," *IEEE Trans. Ind. Appl.*, vol. 45, no. 4, pp. 1368–1377, Jul./Aug. 2009.

[2] P.-D. Pfister, and Y. Perriard, "Very-high-speed slotless permanent magnet motors: Analytical modeling, optimization, design, and torque measurement methods," *IEEE Trans. Ind. Electron.*, vol. 57, no. 1, pp. 296–303, Jan–2010,

[3] A. Borisavljević, H. Polinder, and J. A. Ferreira, "On the speed limits of permanent-magnet machines," *IEEE Trans. Ind. Electron.*, vol. 57, no. 1, pp. 220–227, Jan. 2010,

[4] M. A. Rahman, A. Chiba, and T. Fukao, "Super high speed electrical machines—Summary," in *Proc. IEEE Power Eng. Soc. General Meet.*, Jun. 2004, vol. 2, pp. 1272–1275.

[5] A. Binder, and T. Schneider, "High-speed inverter-fed AC drives," in *Proc. Int. Aegean Conf. Electr. Mach. Power Electron.*, Sep. 2007, pp. 9–16.

[6] T. Baumgartner, A. Looser, C. Zwyssig, and J. W. Kolar, "Novel high-speed Lorentz-type slotless self-bearing motor," in *Proc. IEEE Energy Convers. Congr. Expo.*, Sep. 2010, pp. 3971–3977.

[7] T. Baumgartner, R. Burkart, and J. W. Kolar, "Analysis and design of a 300-W 500 000-r/min slotless self-bearing permanent-magnet motor," *IEEE Trans. Ind. Electron.*, vol. 61, no. 8, pp. 4326–4336, Aug. 2014,

[8] B. Kenny, P. Kascak, R. Jansen, T. Dever, and W. Santiago, "Control of a high-speed flywheel system for energy storage in space applications," *IEEE Trans. Ind. Appl.*, vol. 41, no. 4, pp. 1029–1038, Jul./Aug. 2005,

[9] M. Kimman, H. Langen, and R. M. Schmidt, "A miniature milling spindle with active magnetic bearings," *Mechatronics*, vol. 20, no. 2, pp. 224–235, 2010.

[10] F. Betschon, "Design principles of integrated magnetic bearings," Ph.D. dissertation, Dept. Inf. Technol. Electr. Eng., ETH Zurich, Zurich, Switzerland, 2000.

[11] P. Imoberdorf, "Ultrakompakter Antrieb mit radial und axial kombiniertem Magnetlager," Ph.D. dissertation, Dept. Inf. Technol. Electr. Eng., ETH Zurich, Zurich, Switzerland, 2011.
[12] S. Silber, J. Sloupensky, P. Dirnberger, M. Moravec, M. Reisinger, and W. Amrhein, "High speed drive for textile rotor spinning applications," *IEEE Trans. Ind. Electron.*, vol. 61, no. 6, pp. 2990–2997, Jun. 2014,
[13] G. Schweitzer, and E. H. Maslen, *Magnetic Bearings*. New York, NY, USA: Springer, 2009.
[14] H.-Y. Kim, and C.-W. Lee, "Analysis of eddy-current loss for design of small active magnetic bearings with solid core and rotor," *IEEE Trans. Magn.*, vol. 40, no. 5, pp. 3293–3301, Sep. 2004,
[15] H. Mitterhofer, W. Gruber, and W. Amrhein, "On the high speed capacity of bearingless drives," *IEEE Trans. Ind. Electron.*, vol. 61, no. 6, pp. 3119–3126, Jun. 2014,
[16] Y. Okada, H. Konishi, H. Kanebako, and C.-W. Lee, "Lorentz force type self-bearing motor," in *Proc. 7th Int. Symp. Magn. Bearing.*, 2000, pp. 353–358.
[17] D. Kim and L. Stephens, "Fault tolerance of a lorentz-type slotless self-bearing motor according to the coiling schemes," in *Proc. 7th Int. Symp. Magn. Bearings*, 2000, pp. 219–224.
[18] Z. Ren, and L. Stephens, "Force characteristics and gain determination for a slotless self-bearing motor," *IEEE Trans. Magn.*, vol. 42, no. 7, pp. 1849–1860, Jul. 2006,
[19] T. Grochmal, and A. Lynch, "Control of a self-bearing servomotor," *IEEE Control Syst.*, vol. 29, no. 5, pp. 74–92, Oct. 2009,
[20] H.-I. Lee, S.-Y. Yoo, and M. Noh, "Toroidally-wound self-bearing BLDC motor with Lorentz force," *IEEE Trans. Magn.*, vol. 46, no. 6, pp. 2148–2151, Jun. 2010,
[21] S. Ueno, S.-i. Uematsu, and T. Kato, "Development of a Lorentz-force-type slotless self-bearing motor," *J. Syst. Design Dyn.*, vol. 3, no. 4, pp. 462–470, 2009.
[22] R. P. Jastrzebski, and R. Pllnen, "Centralized optimal position control for active magnetic bearings: Comparison with decentralized control," *Electr. Eng.*, vol. 91, pp. 101–114, Jul. 2009,
[23] W. Zhang, and Y. Hu, "A prototype of flywheel energy storage system suspended by active magnetic bearings with PID controller," in *Proc. IEEE Asia-Pacific Power Energy Eng. Conf.*, Mar. 2009, pp. 1–4.
[24] H.-C. Chen, "Adaptive genetic algorithm based optimal PID controller design of an active magnetic bearing system," in *Proc. 3rd IEEE Int. Conf. Innovative Comput. Inform. Contro.*, Jun. 2008, pp. 603-1–603-8.
[25] R.-J. Wai, J.-D. Lee, and K.-L. Chuang, "Real-time PID control strategy for maglev transportation system via particle swarm optimization," *IEEE Trans. Ind. Electron.*, vol. 58, no. 2, pp. 629–646, Feb. 2011,
[26] T. Schuhmann, W. Hofmann, and R. Werner, "Improving operational performance of active magnetic bearings using Kalman filter and state feedback control," *IEEE Trans. Ind. Electron.*, vol. 59, no. 2, pp. 821–829, Feb. 2012,
[27] R. P. Jastrzebski, "Design and implementation of FPGA-based LQ control of active magnetic bearings," Ph.D. dissertation, Dept. Electr. Eng., Lappeenranta Univ. Technol., Lappeenranta, Finland, 2007.
[28] H.-Y. Kim, and C.-W. Lee, "Design and control of active magnetic bearing system with Lorentz force-type axial actuator," *Mechatronic.*, vol. 16, no. 1, pp. 13–20, Feb. 2006,
[29] M. Ahrens, L. Kucera, and R. Larsonneur, "Performance of a magnetically suspended flywheel energy storage device," *IEEE Trans. Control Syst. Technol.*, vol. 4, no. 5, pp. 494–502, Sep. 1996,
[30] J. W. Beams, J. L. Young, and J. W. Moore, "The production of high centrifugal fields," *J. Appl. Phys.*, vol. 17, pp. 886–890, Apr. 1946,
[31] A. Boletis and H. Bleuler, "Three axis AMB high speed micro motor," in *Proc. 9th Int. Symp. Magn. Bearings*, Aug. 2004, pp. 1–6.
[32] T. Reichert, T. Nussbaumer, and J. W. Kolar, "Complete analytical solution of electromagnetic field problem of high-speed spinning ball," *J. Appl. Phys.*, vol. 112, pp. 104901-1–104901-9, Nov. 2012,
[33] B. E. Kane, "Levitated spinning graphene flakes in an electric quadrupole ion trap," *Phys. Rev.*, vol. 82, pp. 115441-1–11 544-13, Sep. 2010,
[34] T. Baumgartner, and J. W. Kolar, "Multivariable state feedback control of a 500 000 rpm self-bearing motor," in *Proc. IEEE Int. Electr. Mach. Drives Conf.*, May. 2013, pp. 366–372.
[35] A. Looser, T. Baumgartner, J. W. Kolar, and C. Zwyssig, "Analysis and measurement of three-dimensional torque and forces for slotless permanent-magnet motors," *IEEE Trans. Ind. Appl.*, vol. 48, no. 4, pp. 1258–1266, Jul./Aug. 2012.
[36] A. Muesing, C. Zingerli, P. Imoberdorf, and J. W. Kolar, "PEEC-based numerical optimization of compact radial position sensors for active magnetic bearings," in *Proc. 5th IEEE Int. Conf. Integr. Power Syst.*, Mar. 2008, pp. 1–5.
[37] S. Skogestad, and I. Postlethwaite, *Multivariable Feedback Control: Analysis and Design.*, 2nd ed. New York, NY, USA: Wiley, 2005.
[38] R. Larsonneur, "Design and control of active magnetic bearing systems for high speed rotation," Ph.D. dissertation, Dept. Mech. Process Eng., ETH Zurich, Zurich, Switzerland, 1990.
[39] R. Craig, and A. Kurdila, *Fundamentals of Structural Dynamics*. New York, NY, USA: Wiley, 2011.
[40] H. Khalil, *Nonlinear Systems*. Englewood Cliffs, NJ, USA: Prentice-Hall, 2002.
[41] R. Herzog, P. Buhler, C. Gahler, and R. Larsonneur, "Unbalance compensation using generalized notch filters in the multivariable feedback of magnetic bearings," *IEEE Trans. Control Syst. Technol.*, vol. 4, no. 5, pp. 580–586, Sep–1996,
[42] H. Mitterhofer, and W. Amrhein, "Motion control strategy and operational behavior of a high speed bearingless disc drive," in *Proc. 6th IEEE IET Int. Conf. Power Electron., Mach. Drive.*, Mar. 2012, pp. 1–6.
[43] R. Isermann, and M. Munchhof, *Identification of Dynamic Systems*. New York, NY, USA: Springer, 2001.
[44] T. Baumgartner, "A magnetically levitated 500 000 rpm electrical drive system," Ph.D. dissertation, Dept. Inf. Technol. Electr. Eng., ETH Zurich, Zurich, Switzerland, 2013.

Thomas Baumgartner (S'10) received the M.Sc. and Ph.D. degrees in electrical engineering from the Swiss Federal Institute of Technology (ETH) Zurich, Zurich, Switzerland, in 2009 and 2013, respectively.

He was with the Automatic Control Laboratory at ETH Zurich, where he was involved in the field of trajectory prediction algorithms for low-cost collision avoidance systems. From 2009 to 2013, he was with the Power Electronic Systems Laboratory, working on magnetic bearings for ultra-high-speed drive systems. Since 2013, he has been a flight test engineer for the Swiss Government.

Johann W. Kolar (M'89–SM'04–F'10) received the M.Sc. and Ph.D. degrees *(summa cum laude/ promotio sub auspiciis praesidentis rei publicae)* from the Vienna University of Technology, Vienna, Austria.

Since February 1, 2001, he has been a Professor and the Head of the Power Electronic Systems Laboratory, Swiss Federal Institute of Technology (ETH) Zurich, Zurich, Switzerland. He has proposed numerous novel pulse width modulation converter topologies and modulation and control concepts, e.g., the Vienna Rectifier, the Swiss Rectifier, and the Three-Phase AC/AC Sparse Matrix Converter. He has published more than 600 scientific papers in international journals and conference proceedings and filed more than 110 patents.